Mixed-Functionalized Sc_2CT_x (T = O, OH, F) *MX*ene for Electrocatalytic CO_2 Reduction: Insight from First-Principles Calculations

Asha Yadav,[1] Vikram,[1,2] Nirpendra Singh,[3,4] and Aftab Alam[1,*]

[1] *Department of Physics, Indian Institute of Technology, Bombay, Powai, Mumbai 400076, India*
[2] *Department of Chemistry, University of Reading, Whiteknights, Reading RG6 6AD, United Kingdom*
[3] *Department of Physics, Khalifa University of Science and Technology, Abu Dhabi 127788, United Arab Emirates*
[4] *Center for Catalyst and Separation, Khalifa University of Science and Technology, Abu Dhabi 127788, United Arab Emirates*

(Received 21 December 2021; revised 1 July 2022; accepted 5 July 2022; published 8 August 2022)

A microscopic understanding of the mixed-functionalized *MX*enes ($M_2X - T_x$; T_x = O, OH, and F) are extremely important to the design of efficient CO_2 catalytic activity. Here, we report a first-principles study of the CO_2 activation on pure O, OH, and F and mixed-functionalized Sc_2C *MX*ene surfaces. We find that CO_2 adsorption energy can be tuned by changing the coverage of O, OH, and F functional groups on the surface. Fully terminated O and F Sc_2C forms weak interactions with CO_2 molecules (binding energy -0.136 and -0.168 eV) whereas mixed-functionalized Sc_2C surface exhibits higher binding energy(-0.364 eV). In the mixed-functionalized Sc_2C case, only O sites allow CO_2 reduction (F and OH are inactive) and finally converts into methane (CH_4). *Ab-initio*-based Bader charge analysis and projected density of state calculations reveal strong bonding between the C atom of CO_2 and O functional group. The Gibbs free-energy calculation confirms the conversion of HCO into H_2CO to be a rate-limiting step with the limiting potential 1.387 eV. In the mixed-functionalized surface, as we increase the number of OH groups in the vicinity of O sites, the binding energy increases (transiting from a physisorption to a chemisorption regime). However, increasing the amount of O coverage turns out to be detrimental to the catalytic activity. Our study highlights the role of different functional groups in achieving efficient CO_2 catalytic activity on Sc_2C *MX*ene, which can further help us to design experiments accordingly.

DOI: 10.1103/PhysRevApplied.18.024020

I. INTRODUCTION

Photo/electrochemical CO_2 reduction reaction (CO_2RR) is one of the main potential methods to convert CO_2 into value-added chemicals and fuel products [1]. Yet, this is also a challenging reaction due to the linear and highly stable structure of CO_2 molecules. The dissociation energy of the C=O bond is 750 kJ/mol, much higher than that for C−H (430 kJ/mol) and C−C (336 kJ/mol). This implies that a large amount of energy will be required for CO_2 to convert into formic acid, methane, and methanol [2]. Thus, several efforts have been taken to develop efficient catalysts for the photo/electrochemical CO_2RR [3] but expanding the technology to an industrial scale is still far away [4–10]. Despite the widespread efforts to develop efficient catalysts for CO_2RR, there still exists several challenges such as high overpotential, high activation energy, low energy efficiency, low selectivity, and high onset potential [7,11].

Cu metal has been a benchmark for electrochemical CO_2RR [7,12–14]. Inspired from this, several other catalysts have been proposed for CO_2RR [10,15]. Nevertheless, lower catalytic performance, high overpotential, and low product selectivity has made these materials unsuitable for industrial purposes. *MX*enes (2D transition metal carbide/nitride) are relatively new class of materials which have been synthesized recently by selective HF/HCl chemical etching of the *A* layer from *MAX* phases (here *M* represents transition metal, *A* represents IIIA/IVA elements, and *X* is C or N)]. The chemical etching of *MAX* phases results in oxygen (O), hydroxyl (OH), and fluorine (F) terminated *MX*ene [16–20] and have lower surface energy compared with bare *MX*ene surface [21]. High surface area and excellent chemical and mechanical stability make *MX*enes extremely suitable for wide array of applications such as energy storage involving supercapacitors [22], batteries [22], and water splitting [23]. In the last few years, several interesting studies have been presented on these and related materials which suggest that it could be a potential candidate for electrochemical CO_2RR [24]. However, these studies involve either bare *MX*enes or

*aftab@iitb.ac.in

monofunctionalized surface for CO_2RR studies. For example, 2D M_3C_2-type *MX*enes (M =Sc, V, Cr, Mn, Zr, Nb, Mo, Mo_2Ti, Hf, Ta, and W) have been explored towards CO_2RR for CH_4 conversion using a first-principles method [25]. The IV, V, and VI group-based M_2C *MX*enes are investigated to understand their electrocatalytic activities [26]. The study on bare IV, V, and VI group M_3C_2 *MX*enes for CO_2RR [27] suggests Mo_3C_2 and Cr_3C_2 to be the most promising catalysts with limiting potentials of 1.05 and 1.31 V, respectively, and further reduced to 0.35 and 0.54 eV by the addition of an O or OH group. There are also a few studies using density functional theory (DFT) calculations which revealed the role of O- or OH-functionalization towards CO_2RR processes [26,28,29].

It is well known, both theoretically [21] and experimentally (chemical etching method) [16–19], that mixed-functionalized surfaces are more stable and likely to form in a real system. Despite all the theoretical investigations, mixed-functionalized surface studies are extremely limited [30]. We found only a single report which depicted the two (O+F) functionalized *MX*ene surfaces for CO_2RR [31]. According to this study, Ti- and Mo-based catalyst surfaces show that the O+F terminated surface with lower amounts of F termination gives better activity compared with high F terminated surfaces [31]. Thus, it can be suspected that the presence of mixed functional group has a crucial effect on surface properties. From the point of view of CO_2RR, CO_2 activation at catalyst is a vital and challenging task. In this regard, surface morphology has crucial influence on CO_2 activation. This is exemplified in several systems where intrinsic defects and the electron/atom (e/a) ratio sensitively dictates CO_2 adsorption (chemisorption and physisorption) processes [32–35]. Thus, a deeper insight into these aspects of CO_2 activation on the mixed-functionalized surface of *MX*enes is highly desirable which can guide future experiments to achieve more efficient catalyst for CO_2RR.

In this report, we perform a detailed investigation of the electrocatalytic CO_2RR activity of mixed-functionalized (F, O, OH) Sc_2C *MX*ene, which is a more realistic choice of surface for catalytic process. The study unfolds various distinctive chemical features of mixed-functionalized surface as compared with the unmixed ones when CO_2 is adsorbed. Apart from a significant effect on the binding energy of the CO_2, a careful analysis of mixed-functionalized Sc_2C *MX*ene reveals that HCO to H_2CO conversion is the rate limiting step. Our *Ab initio* simulation shows that the O-site acts as an active site for CO_2 adsorption whereas the presence of OH group improves CO_2 binding. It was found that as we increase the clustering of OH group in the vicinity of the active O-site, the binding energy increases rapidly. The present work categorically explains the response of each functional group during CO_2 activation process thus provides an effective way to modulate the surface terminations and, hence, to obtain the most efficient catalyst for CO_2RR

II. COMPUTATIONAL DETAILS

The first-principles calculations are carried out using DFT as implemented in Vienna *Ab initio* Simulation Package (VASP) code [36,37]. The generalized gradient approximation [38] with Perdue-Burke-Ernzerhof (PBE) [39] is employed to capture the exchange and correlation effects. The electron-ion interaction is incorporated within the projector augmented wave (PAW) method [40] with an energy cutoff of 500 eV. The Γ-centered Monkhorst-Pack $9 \times 9 \times 1$ k-mesh is used for the Brillioun zone integration [41,42]. The force (energy) is converged up to a tolerance level of 0.05 eV/Å(10^{-7} eV). The Bader charge analysis is performed using the method developed by Henkelman [43,44]. The van der Waals correction (DFT-D3) [45,46] is included in all the calculations. A 4×4 supercell of Sc_2C slab and a vacuum of 15 Åalong z direction is used for catalysis-based simulation.

The stability of functionalized Sc_2C surface is evaluated by calculating the formation energy

$$\Delta H_f = E_{\text{tot}}(Sc_2CT_n) - E_{\text{tot}}(Sc_2C) - (n/2)E_{\text{tot}}(T_2), \quad (1)$$

where $E_{\text{tot}}(Sc_2CT_n)$ and $E_{\text{tot}}(Sc_2C)$ represent the total energy of functionalized and bare Sc_2C surface. Here, T_n = O, OH, F groups, hence $E_{\text{tot}}(T_2)$ corresponds to total energy of F_2, O_2+H_2, or O_2.

The surface energy (γ) of bare and functionalized Sc_2C are calculated using the expression

$$\gamma = \frac{1}{2A}\left(E_{\text{slab}} - \sum_i n_i\mu_i\right), \quad (2)$$

where E_{slab} is the total energy of the slab, and n_i and μ_i are the number of species in the slab and their chemical potential. The fraction represents two sides of slab. A represents surface area of the slab.

The adsorption energy is computed using the following formula,

$$E_{\text{ads}} = E_{\text{adsorbate@slab}} - E_{\text{slab}} - E_{\text{adsorbate}} \quad (3)$$

where E_{ads} is the adsorption energy CO_2 and other intermediates observed during reduction process, $E_{\text{adsorbate@slab}}$, E_{slab}, and $E_{\text{adsorbate}}$ are the total energies of the molecules adsorbed on the surface, surface slab, and free adsorbate molecule, respectively. The adsorption energies of intermediates are calculated using the total energy of the intermediate molecules in gas phase. The gas molecules employed for calculations are $1/2H_2$, H_2O, HCOOH, H_2CO, CH_3OH, and CH_4.

The free energy of the CO_2 reduction process is calculated using the computational hydrogen electrode model [47]. The chemical potential of the H^+/e^- pair is equal to half of the chemical potential of the H_2 molecule under standard conditions (pH = 0, fugacity $f(H_2)$ = 101,325 Pa, T = 298 K). The free energy of each system can be obtain using $G = E_{DFT} + ZPE - TS$. Here, E_{DFT} is the total electronic energy of each species obtained using DFT calculation, ZPE is the zero-point energy, T is temperature, and S is entropy. ZPE can be given by ZPE = $1/2h\nu_i$, where h is Planck's constant and ν_i is vibrational frequency. The S correction can be expressed as a sum of electronic (S_e), translational (S_t), rotational (S_r), and vibrational (S_v) term:

$$S = S_e + S_t + S_r + S_v. \tag{4}$$

At the fundamental electronic level S_e becomes 0. For molecular species, major contributions come from translational, rotational, and vibrational terms, whereas for solids both S_t and S_r become negligible. For both ZPE and S, the contribution from vibration is computed using phonon calculations. Consequently, the change in Gibbs free energy of each step of the CO_2 reduction reaction are calculated using $G = E_{DFT} + ZPE - TS$ and $\Delta G = \Delta E_{DFT} + \Delta ZPE - T\Delta S + eU$, where ΔE_{DFT} is the change in total energy between reactants and products (adsorption energy). Here ΔZPE and $T\Delta S$ are the change in the zero-point energy correction and vibrational entropy, respectively, at room temperature and e and U are the number of electrons transferred and applied potential for each step. We use $U = 0$ eV for free energy calculation at equilibrium. The liming potential is the energy required to make all the elementary steps exergonic is determined by $U_L = -\Delta G_{max}/e$, where ΔG_{max} is the most positive value of change in free energy.

III. RESULTS AND DISCUSSION

The bare Sc_2C and functionalized Sc_2C *MX*enes are usually extracted from hexagonal bulk Sc_2AlC unit cell possessing $P6_3/mmc$ symmetry. The structure of the later is shown in Fig. 1(a). The optimized lattice parameters of Sc_2AlC are $a = b = 3.29$ Å and $c = 15.15$ Å which match fairly well with the previous report [48]. Figure 1(b) shows bare Sc_2C which consists of a carbon layer as a middle layer sandwich between two Sc layers. From top view, H1 and H2 correspond to hollow sites just above Sc and C atoms, respectively. We first simulated the 100% coverage of each functional groups (F/O/OH) at H1 and H2 sites of Sc_2C *MX*ene surface [see Fig. 1(c)]. The O, OH, and F functionalization occupying H1 site is referred to as Sc_2C–O, Sc_2C–OH, and Sc_2C–F, whereas geometry with H2-site occupancy is referred as Sc_2C–O_b, Sc_2C–OH_b, and Sc_2C–F_b, respectively. On the basis of total energy it was found that F and OH prefer to occupy the H1 site, whereas O prefers to occupy the H2 site (see Table S1 of the Supplemental Material [50]) which is consistent with previous reports [49].

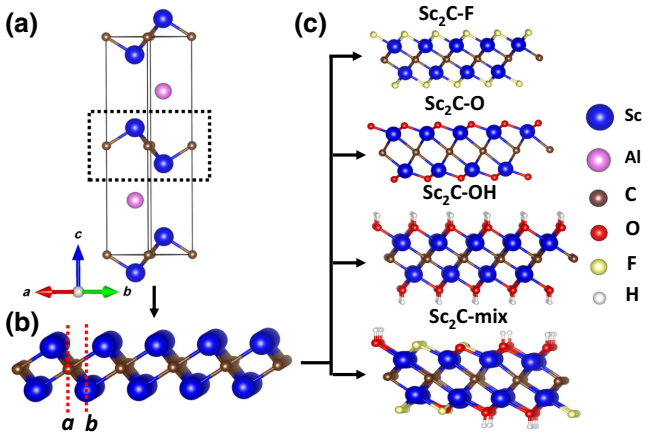

FIG. 1. Schematic side view of optimized (a) bulk Sc_2AlC, (b) 4×4 supercell of Sc_2C, and (c) different functionalized Sc_2C surfaces. The black dotted line in (a) shows the cleaved portion of bulk Sc_2AlC unit cell whereas red dashed lines in (b) indicate the position of two hollow sites (H1 and H2) for O, OH, and F adsorption.

To study the effect of mixed functionalization on *MX*ene surface, we considered a coverage of 34.375% F (11 out of 32 sites), 34.375% OH (11 out of 32 sites), and 31.250% O (10 out of 32 sites). This is labeled as "Sc_2C-mix" and shown in Fig. 1(c). Following Ref. [21] we constructed Sc_2C-mix using approximately equal coverage of functional groups, i.e., 10 O, 11 OH, and 11 F atoms. In the later section, we varied the amount of O functional. For the construction we placed five O, five OH groups, and six F atoms on the top side [as shown in the Fig. S1(a) of the Supplemental Material [50]] whereas five O, six OH, and five F were placed on the bottom side. This is the simplest configuration where four F, four OH, and four O are adsorbed in the adjacent line, whereas the remaining OH, O, and F atoms were placed on the next line (see Fig. S1(a) of the Supplemental Material [50]). Next, to check the effect of changing the order of alignment of O–OH–F, we designed three more configurations maintaining the same stoichiometry of O, OH, and F atoms. These are shown in Figs. S1(b)–(d) of the Supplemental Material [50]. Interestingly, the energetics of all these configurations remain close to each other (within 1 meV/atom). In the present work, the energetically most stable configuration is chosen for more detailed study. Apart from this, two more configurations of Sc_2C-mix were created, one where all O, OH and F occupy the H1 site and the other ''Sc_2C-mix(b)" where F and OH sit at the H1 site whereas O atoms sit at the H2 site. The optimized "Sc_2C-mix" (all O, OH, and F at the H1 site) configuration is considered

TABLE I. Formation and Surface energy of bare Sc_2C, $Sc_2C{-}O_b$, $Sc_2C{-}OH$, $Sc_2C{-}F$, and Sc_2C-mix (34.374% F, 34.375% OH, and 31.250% O).

Slab model	Formation energy (eV/atom)	Surface energy (meV/Å^2)
Sc_2C	–	29.6
$Sc_2C{-}F$	−2.359	−596.4
$Sc_2C{-}O_b$	−1.667	−411.1
$Sc_2C{-}OH$	−1.440	−491.0
Sc_2C-mix	−2.026	−510.0

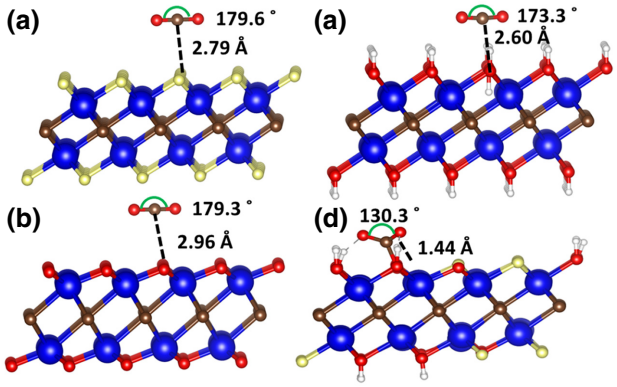

FIG. 2. Optimized configuration of CO_2 adsorbed on (a) $Sc_2C{-}F$, (b) $Sc_2C{-}O$, (c) $Sc_2C{-}OH$, and (d) Sc_2C-mix terminated surfaces. The blue, brown, yellow, red, and white spheres are Sc, C, F, O, and H atoms.

for further investigation because it exhibits lower energy compared with Sc_2C-mix(b). Figure S2 of the Supplemental Material [50] displays the total density of states (DOS) of Sc_2C–F, Sc_2C–O, Sc_2C–OH, and Sc_2C-mix using the PBE functional. The purely F and OH terminated Sc_2C turn out to be semiconducting with band gaps of 0.97 and 0.98 eV, respectively, whereas O terminated Sc_2C and Sc_2C-mix are metallic, which matches with a previous report [49]. Functionalized Sc_2C turns out to have lower surface and formation energies as compared with the bare version, as listed in Table I. The formation energies of the functionalized surfaces follow a certain trend, in the order of $Sc_2C{-}O < Sc_2C{-}OH < Sc_2C$-mix $< Sc_2C{-}F$, with large negative values indicating strong bond formation between Sc and O/OH/F, consistent with a previous report [51]. The lower surface energy of all the functionalized surfaces compared with bare Sc_2C engenders the stability/formation of functionalized surface. High negative value of formation and surface energy of $Sc_2C{-}F$ suggest F functionalization to be most favorable at 0 K. However, depending on the temperature and synthesis environment, the relative stability of different functionalization groups may vary, as evidenced experimentally [15–19].

Next, the CO_2 molecule is placed over different functionalized Sc_2C surfaces and the structures were relaxed. The optimized structures show some reconstruction. The relaxed bond distance ($C_{CO_2}{-}O_{Sc_2}C$) between the CO_2 molecule and O, F, and O_{OH} (O of OH group) of $Sc_2C{-}F$, $Sc_2C{-}O$, and $Sc_2C{-}OH$ surface [as shown in Figs. 1(a)–1(c)] turn out to be 2.79, 2.96, and 2.60 Å, respectively. In the case of $Sc_2C{-}F$, $Sc_2C{-}O$, and $Sc_2C{-}OH$ there is no major change in the bond angle of the CO_2 molecule observed after relaxation as indicated in Table II. To further confirm CO_2 binding on Sc_2C-OH, the adsorption of CO_2 molecule at different positions was checked. For example, CO_2 molecule was placed above the H atom in an inverted-V shape making bond between O of CO_2 molecule and H of OH group (as shown in Fig. S3 of the Supplemental Material [50]), and then relaxed. After optimization, even this configuration does not show any significant interaction between CO_2 molecule and $Sc_2C{-}OH$ surface. Out of various such possible configurations, the configuration shown in Fig. 2(c) is energetically the most stable. Interestingly, the mixed-functionalized surface "Sc_2C-mix" results in bending of the linear CO_2 molecule into V-shape with the bond angle transition from 180° (gaseous CO_2 molecule) to 130.3° [see Fig. 2(d)]. The bond length between O_{Sc} (O of Sc_2C-mix) and C_{CO_2} (C of CO_2) is also affected drastically (1.44 Å) bringing the CO_2 molecule much closer to the Sc_2C surface [see Fig. 2(d)].

The enhanced CO_2 activation on Sc_2C-mix surface further leads to O=C and C=O bond elongation (1.267 and 1.247 Åfrom 1.176 Å), thus weakening C–O bonding. This is further confirmed by a charge transfer of $0.321|e|$ from Sc_2C-mix surface to CO_2 molecule, mediating the formation of anionic $CO_2^{\delta-}$. Figure S4 of the Supplemental Material [50] shows the atom/orbital projected DOS of molecular orbitals ($1\pi_g$, $2\pi_u$) of CO_2 in free and adsorbed states. The molecular orbital has significant change in the orbital distribution near the Fermi level. Comparison between the atom/orbital DOS of C-p and O-p of CO_2 molecule and O_{Sc}-p orbital of Sc_2C-mix surface shows strong hybridization, further confirming the CO_2 activation at O_{Sc} of Sc_2C-mix. The CO_2 prefers physisorption with the adsorption energy −0.135 and −0.168 eV when placed at F and O sites, respectively (listed in Table II), whereas in the case of OH, CO_2 adsorbs with a binding energy of 0.748 eV hinting towards an endergonic process. The moderate displacement of the H atom of the OH group from its original position is also an indication of the possibility of an endergonic process. This can be clearly seen in Fig. 2(c). Thus, one can conclude that the interaction of CO_2 molecule with Sc_2C-OH surface is mediated by C_{CO_2} and O_{OH}.

As mixed-functionalized *MX*enes are more likely to form during the experimental synthesis, we chose the Sc_2C-mix configuration for further investigation of CO_2 to CH_4 conversion. The product selectivity strongly depends

TABLE II. Bond distance between $C_{CO_2}-O_b$, $C_{CO_2}-OH$, and C_{CO_2}–F of Sc_2C surface, CO_2 bond angle, and binding energy CO_2 adsorbed surface with different terminations.

Configurations	Bond distance between $C_{CO_2}-$O/OH/F of Sc_2C surface (Å)	O–C–O bond angle (deg)	Binding energy (eV)
Sc_2C-F	2.79	179.6	−0.135
Sc_2C-O_b	2.96	179.3	−0.168
Sc_2C-OH	2.60	173.3	0.748
Sc_2C-mix	1.44	130.3	−0.364

on subsequent elementary steps and adsorption energy of reaction intermediates formed. In this regard, the Gibbs free energies of different reaction intermediates formed during the subsequent electron coupled protonation steps on Sc_2C-mix at room temperature is an important descriptor. This is displayed in Fig. 3. In general, for the first hydrogenation (H^+/e^-) step, there are two possible sites, namely C and O of CO_2 molecules where H atom can attack resulting in the formation of *COOH or *HCOO (see Fig. 4), where * indicates the boundedness of CO_2 and its intermediates on Sc_2C-mix surface. However, in the Sc_2C-mix case, CO_2 gets adsorbed via the formation of $C_{CO_2} - O_{Sc}$ bond thus endows both the O of CO_2 slightly above the surface plane. Owing to the steric advantage associated with O_{CO_2}, the (H^+/e^-) attacking both the oxygen is more favorable in comparison with C_{CO_2} site. Our calculations also show that H prefers to bind at the O site and converts CO_2 into *COOH with an adsorption energy of −0.80 eV, indicating the exergonic nature of the reaction (Fig. 3). In contrast to this, CO_2 adsorption on bare M_2C *MX*enes (M = IV, V, and VI transition metal) reported by GuO *et al.* [25] shows O_{CO_2}–M bond formation, whereas the C atom of CO_2 remains slightly above the basal plane. Owing to the steric advantage with C of CO_2 in the case of bare M_2C-*MX*ene, formation of *OHCO is found to be energetically favorable on first hydrogenation in contrary to the present scenario. Thus, this study further depicts that the surface functionalization has crucial effect on CO_2 binding and the formation of reaction intermediates. The generated *COOH further undergoes reduction by H^+/e^-. The H^+/e^- attacking at O of the OH site (present in *COOH) can form CO with the removal of H_2O, whereas if it attacks at the C site this can result in *HCOOH; a reaction usually observed in metal, metal oxide/chalcogenides catalysts [11,33,34]. Interestingly, the CO_2 adsorption at the O_{Sc} site of the functionalized surface is distinctly different as compared with the corresponding reaction on bare metal catalysts [10,11,24,25] because of the formation of three C–O bonds (one $C-O_{Sc}$ and two $C-O_{CO_2}$) in the former as opposed to two. Thus, conversion of $COO_{Sc}OH$ into CO by formation of H_2O molecule is difficult and it results in reverse CO_2 evolution. Our calculations show that the reaction for reverse formation of CO_2 is less favorable (by 0.58 eV) as compared with subsequent *$HCOO_{Sc}OH$ formation with a binding energy of 0.41 eV, which suggests endergonic nature. Hence, for further calculation we proceed with *$HCOO_{Sc}OH$. After the first hydrogenation, $C-O_{Sc}$ distance decreases, which can also be inferred from the binding energy value that increase from −0.37 to −0.80 eV. With the second hydrogenation (hydrogenation of COOH), $C-O_{Sc}$ bond length increases to 1.46 Å. In the next hydrogenation step, H_2O removal results in stronger *$HCOO_{Sc}$ binding energy (−3.016 eV) indicating exergonic reaction (as shown in Fig. 3). The enhanced binding energy mainly attributed to C–O bond breaking and removal of H_2O leads to enhanced $C-O_{Sc}$ interaction. The change in the free energy required for conversion of *$HCOO_{Sc}$ into *$HCOO_{Sc}H$ (formic acid) and

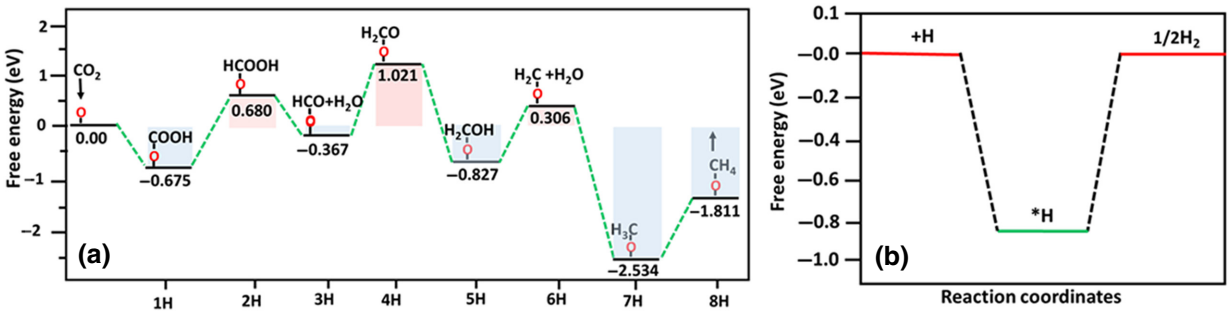

FIG. 3. (a) Calculated free energy of the reaction pathway starting from CO_2 adsorbed Sc_2C-mix surface. Here, red colored O refers to O_{Sc} of the functionalized surface. Blue and pink shaded region indicates exergonic and endergonic process. (b) Change in free energy for the hydrogen evolution reaction on Sc_2C-mix surface.

$*H_2COO_{Sc}$ are 1.20 and 1.02 eV, respectively, indicating H^+/e^- attack at the C site is energetically favorable. The binding energy of $*HCOO_{Sc}H$ is found to be 0.82 eV. The distance between O_{Sc} and Sc_2C surface of Sc_2C-mix itself increases to 2.55 Å (from 2.18 Å). The increased O_{Sc}–Sc bond length indicates $*HCOO_{Sc}H$ is loosely bound to the surface. In other words, this hints towards a possible evolution of $*HCOO_{Sc}H$ during CO_2 reduction reaction which may result in O vacancy on Sc_2C-mix surface.

The H_2COO_{Sc} with binding energy 0.312 eV undergoes a further reduction process with H^+/e^- pair attacking at O site and converting it into $*H_2CO_{Sc}OH$. In the following steps, H^+/e^- can attack either at O_{Sc} or O sites. The hydrogenation at O_{Sc} leads to the formation of methane diol ($CH_2(OH)_2$) with the binding energy +0.85 eV, whereas hydrogenation at O gives out H_2O molecule with strongly bound $*H_2CO_{Sc}$ having a binding energy −3.63 eV. Here, in this step, C bind to another O_{Sc} of Sc_2C-mix surface because of loss of O_{CO_2} in order to complete its valency. The H_2C binds with two O_{Sc} of Sc_2C-mix surface with higher binding strength (binding energy −3.63 eV). Subsequent hydrogenation of H_2C results in continuous attack on the C site of $*H_2CO_{Sc}$ and it converts into $*H_3CO_{Sc}$ and H_4C. Attack of H at O_{Sc} of CH_3O_{Sc} is also checked and it confirms the formation of $CH_3O_{Sc}H$. However, $CH_3O_{Sc}H$ evolution results in further O_{Sc} vacancy. To check the selectivity towards C1 product (compound with 1 carbon atom: CH_4, CH_3OH, CO, HCOOH, etc.) evolution, the binding energies of CH_4 and $CH_3O_{Sc}H$ were calculated which turn out to be 0.52 and 0.74 eV, respectively. Lower binding energy of CH_4 compared with $CH_3O_{Sc}H$, $CH_2(OH)_2$, and $HCOO_{Sc}H$ suggest high selectivity towards CH_4 evolution during CO_2 reduction reaction. Figure 4 displays the free energy diagram which clearly shows that hydrogenation of $*COO_{Sc}OH$, $*HCOO_{Sc}$, and $*H_2CO_{Sc}OH$ is endothermic while the remainder are exothermic reactions. Thus, the conversion of $HCOO_{Sc}$ into H_2COO_{Sc} is the potential liming step with a limiting potential of 1.387 eV.

The hydrogen evolution reaction (HER) is known to be one of the competing reactions during the CO_2 reduction process. We considered HER at different sites of Sc_2C-mix. To initiate HER, H atoms were placed at the O and F sites of Sc_2C-mix. After optimization, it was found that H prefers the O site with HER change in free energy (ΔG_H) of −0.819 eV, whereas H placed at the F site moves to the O site. The lower value of ΔG_H implies that the side reaction HER will be more favorable compared with CO_2 reduction at pH = 0. However, HER also depends on the pH value, hence HER activity can be tuned by changing the pH value.

We explore further to gain a microscopic understanding of the effect of mixed-functionalized group (Sc_2C-mix) on CO_2 activation by varying the amount of O, OH, and F. The CO_2 adsorption on Sc_2C-O shows physisorption. However, in the case of Sc_2C-mix, the CO_2 activation occurs exclusively at O site. Though F and OH of Sc_2C-mix surface does not act as active site for CO_2 activation, the presence of F and OH alters the electronic charge distribution at the surface. The coverage geometry considered so far in Sc_2C-mix surface consists of OH groups sitting at the nearest neighbor of the O_{Sc} site. In reality, however, this may not happen and F and/or O atoms may also occupy the nearest neighbor sites. In order to check the effect of such an environment, we have replaced the OH group at both the nearest neighbors by F and O group, labeled as Sc_2C-mix–F and Sc_2C-mix–O in Fig. 5. The black arrow indicates the sites where OH group was replaced. Replacing the nearest OH by F and O has a crucial effect on the formation energy of Sc_2C-mix–F (−173.3069 eV) and Sc_2C-mix–O (−171.7709 eV), compared with Sc_2C-mix surface (−184.3608 eV). Interestingly, the presence of O and F in place of OH site has a significant effect on CO_2 adsorption. The CO_2 molecule binds with energy −0.291 and −0.297 eV on Sc_2C-mix–F and Sc_2C-mix–O, respectively (as compared with −0.364 eV in the original OH-occupied configuration). This clearly indicates that presence of OH group in the vicinity of O_{Sc} (as an active site) helps to bring the adsorption energy within the moderate chemisorption region. To check the charge transfer mechanism between CO_2 molecule and Sc_2C-mix–F and Sc_2C-mix–O surfaces charge density difference is calculated using [52]

$$\Delta\rho = \rho(CO_2@\text{surface}) - \rho(\text{surface}) - \rho(CO_2), \quad (5)$$

where $\rho(CO_2@\text{surface})$, $\rho(\text{surface})$ and $\rho(CO_2)$ are the charge densities of CO_2 adsorbed on Sc_2C-mix/Sc_2C-mix–F/Sc_2C-mix–O surface, pure Sc_2C-mix/Sc_2C-mix–F/Sc_2C-mix–O surface, and isolated CO_2 molecule, respectively. Figures 5(c) and 5(d) display the charge density difference of the Sc_2C-mix–F, Sc_2C-mix, and Sc_2C-mix–O configurations. The region of charge depletion and accumulation are depicted using cyan and yellow color, respectively.

Among all the three cases, Sc_2C-mix exhibits a significant interaction between H atom of OH group and O of O_{CO_2} which causes a localized charge-deficient region at H atom, whereas F or O atoms do not have any significant contribution. The Bader charge analysis shows a charge transfer of $0.0776|e|$ and $0.0503|e|$ by both the H of OH group (nearest to the active site) to the O_{CO_2} atom. This charge transfer to O_{CO_2} weakens C–O charge sharing. Hence, it is quite plausible that C takes a charge of $0.05|e|$ from O_{Sc} to complete its valency which results in strong interaction between CO_2 and Sc_2C-mix surface, whereas O_{CO_2} does not takes any charge in the other two cases [Figs. 5(c) and 5(e)]. This might be due to the similar electronegativity of O and F. Atom/orbital projected DOS of H of OH group and O of CO_2 molecule located near OH

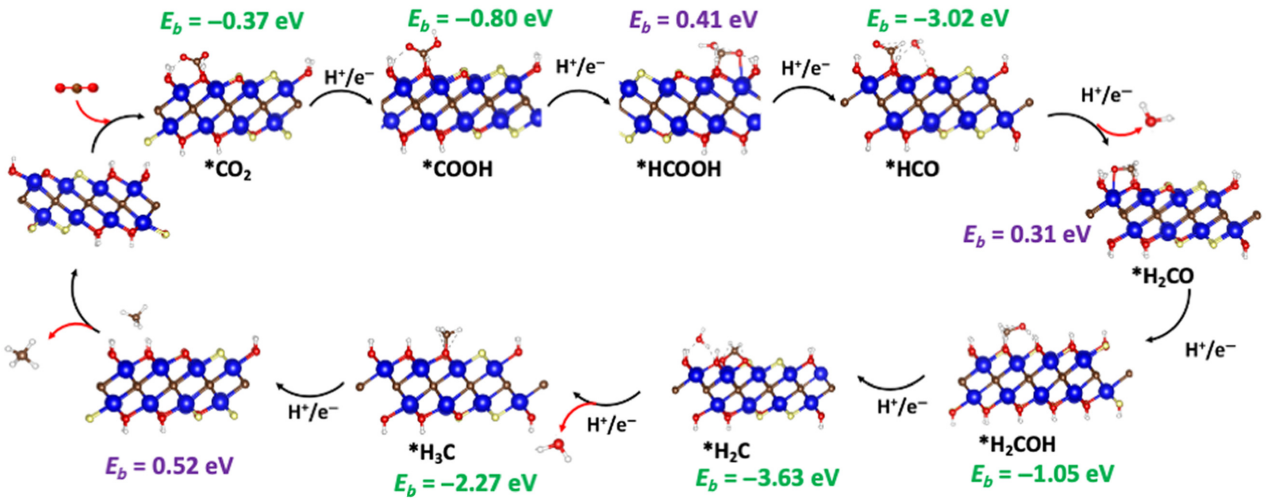

FIG. 4. Proposed CO_2RR mechanism pathway to different products on Sc_2C-mix surface. Here E_b implies binding energy.

functional in Sc_2C-mix is shown in Fig. S5 of the Supplemental Material [50]. This clearly confirms significant hybridization between the two.

We have also evaluated the effect of the number of OH in the vicinity of O_{Sc} (active site) on CO_2 bond angle, $C_{CO_2}-O_{Sc}$ bond length, and CO_2 binding energy. In order to do this, the Sc_2C-mix surface with active O_{Sc} site is taken and all the neighboring sites within a distance 3.27–3.35 Å(see Fig. S6 of the Supplemental Material [50]) are replaced by O atoms. Next, we replaced each O atom by OH one by one and simulate the effects under each environment. Table III lists the change in CO_2 bond angle, $C_{CO_2}-O_{Sc}$ bond length, and CO_2 binding energy with increase in the number of OH group. As the number of OH groups increases from zero to two, the CO_2 bond angle and $C_{CO_2}-O_{Sc}$ bond distance decreases indicating enhanced interaction between CO_2 molecule and Sc_2C-mix surface which is also reflected by the increased binding energy value. Moving from one OH to two OH, CO_2 molecule rotates from first H of OH group (H_{OH}) to middle of first and second H_{OH} atom, as shown in Fig. S7 of the Supplemental Material [50]. Both H_{OH} donate a charge of $0.07|e|$ and $0.06|e|$ to O_{CO_2}. When a third O was replaced by the OH group, O_{CO_2} closer to the third OH rotates towards the third H_{OH} whereas the oxygen near the first and second OH remains unperturbed. In this case O_{CO_2} near the third OH group takes up a charge of $0.074|e|$ from H_{OH}, and increases the binding energy to -0.364 eV. On adding a fourth OH group there is small shift in O_{CO_2} position towards fourth H_{OH}, which in turn causes further increase in CO_2 bond angle with the adsorption energy -0.60 eV. Interestingly, adding a fifth and sixth OH group does not have any significant effect on the bond angle/length but the binding energy increases to -0.682 and -0.750 eV, respectively. After 3OH, further increase of OH content does not show any significant effect on bond angle, however bond distance decreases remarkably suggesting enhanced CO_2 interaction with the surface. This enhanced interaction, in turn, arises due to the sufficient electron (0.05–0.07 e) charge transfer from each H_{OH} to O_{CO_2}. Thus, it can be concluded that addition of first few OH group highly influence O–C–O bond angle due to CO_2 activation. Nevertheless, after two OH groups the change in bond angle crucially depends on O_{CO_2} movement.

Next, we studied the effect of increased oxygen content (from 10 O atoms (31.25%) to 14 O atoms (43.75%) on

TABLE III. Bond distance between C_{CO_2} and O_{Sc} of Sc_2C surface, CO_2 bond angle, and binding energy of Sc_2C-mix with increasing the number of OH group.

Configurations	Bond angle (deg)	$C_{CO_2} - O_{Sc}$ (Å)	Binding energy (eV)
Sc_2C–32O	179.31	2.957	−0.17
Sc_2C-mix with no OH in the nearest neighbor site	177.69	2.878	−0.18
Sc_2C–1OH	177.52	2.891	−0.19
Sc_2C– 2OH	131.96	1.451	−0.29
Sc_2C–3OH	130.21	1.436	−0.36
Sc_2C– 4OH	130.56	1.433	−0.60
Sc_2C–5OH	130.57	1.431	−0.68
Sc_2C– 6OH	130.48	1.430	−0.75

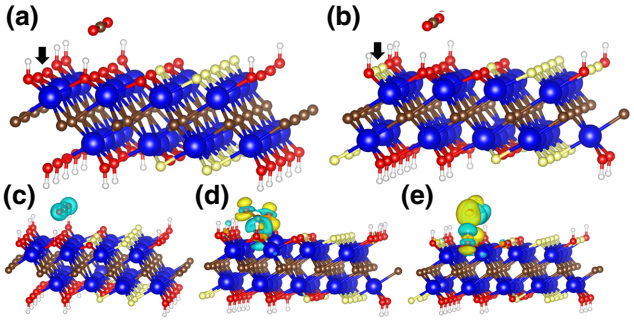

FIG. 5. Optimized configuration of CO_2 adsorbed on (a) Sc_2C–F, (b) Sc_2C–O, (c) Sc_2C–OH, and (d) Sc_2C-mix terminated surfaces. The blue, brown, yellow, and red spheres are Sc, C, F, and O atoms. Here, cyan and yellow region represents charge loss and gain, respectively.

Sc_2C-mix surface) on CO_2 adsorption ability. The fully oxygen functionalized *MX*ene (Sc_2C-O) does not favor CO_2 binding. The Bader charge analysis of mixed and pure F, O, and OH functionalized Sc_2C shows a charge transfer of $0.826|e|$, $1.306|e|$, and $1.101|e|$ from Sc to F, O and O of OH, respectively. Although F is most electronegative, the O atom draws more charge as compared with F atom in order to complete the octet. We also believe that as the coverage by O atoms increases, the charge donation ability of functionalized surface decreases. This is also evident from the DOS plot [see Fig. 6(a)], as the number of states at the Fermi level increases [inset of Fig. 6(a)]. One should note that it is not only the states at the Fermi level that contribute to the charge transfer, but also the lower-energy states modulated by the Fermi-Dirac distribution function (at a given temperature) that play a role. At a given temperature T, the total charge transfer can be calculated as

$$n = \frac{1}{V}\int_{-\infty}^{E_F} f\,(E)g(E)\,dE \tag{6}$$

$$f\,(E) = 1 - F(E) = 1 - \frac{1}{1 + e^{E-E_F/k_BT}} \tag{7}$$

electrons, respectively, is the number of states between energy E and $E + dE$, V is the volume of the cell, and E_F, k_B, and T are the Fermi energy, Boltzmann constant, and temperature in kelvin. The carrier concentration thus evaluated at 300 K for different numbers of O atoms at Sc_2C surface is shown in Fig. 6(b). At 300 K, one can see that carrier concentration decreases as we increase the O termination. It should be noted that this is not a purely O-terminated surface but a mixed-functionalized surface which is used to study the effect on carrier concentration. As our mixed-functionalized surface has 10 O atoms, the trend of increasing it to 14 O atoms is considered, which decreases the carrier concentration as shown. The carrier concentration decreases with increasing oxygen content

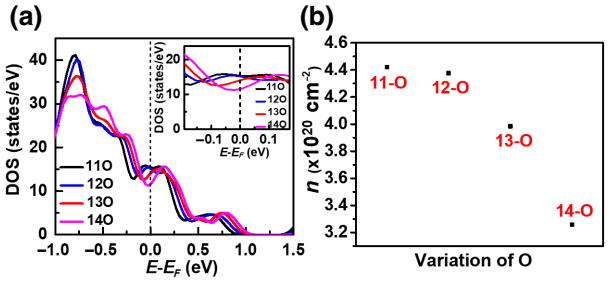

FIG. 6. (a) Total DOS and (b) Carrier concentration versus number of O atoms for different oxygen coverage at 300 K on Sc_2C-mix surface without CO_2 interaction. Here, 11O, 12O, 13O, and 14O represents the number of oxygen atoms.

on Sc_2C-mix surface for a temperature of 300 K, indicating a decreasing ability of charge donation. In short, our comprehensive theoretical study shows that the presence of O termination in a mixed-functionalized (Sc_2C-mix) environment plays a crucial role in catalyzing the CO_2 reduction. It is also observed that when CO_2 is adsorbed on fully OH terminated Sc_2C surface, the CO_2 binds after the formation of H vacancy. We confirm that O atom acts as active site for CO_2 activation. However, the presence of excess oxygen coverage on the surface may be detrimental to CO_2 reduction ability.

IV. CONCLUSIONS

In summary, we have systematically examined the CO_2 catalytic activity of mixed-functionalized (including O, F, and OH group) Sc_2C *MX*ene (labeled as Sc_2C-mix). Purely –F, –O, and –OH terminated surface result in physical adsorption of CO_2 with binding energies of -0.136, -0.168, and 0.748 eV, whereas the mixed-functionalized Sc_2C surface (34.375% F, 34.375% OH, and 31.250% O coverage) results in moderate chemisorption of CO_2 (binding energy of -0.364 eV) with a charge transfer of $0.31|e|$ from Sc_2C-mix to CO_2 molecule. The CO_2 conversion on Sc_2C-mix follows the HCOOH route and eventually converts into CH_4 with reasonably high selectivity. The conversion from HCO to H_2CO is found to be the rate limiting step. The end results are extremely sensitive to the neighboring environment (occupancy of the content and type of functional group) of the active site (oxygen in this case) for CO_2 reduction. For instance, increase in the amount of OH group in the vicinity of O-atom improves the binding energy, which in turn affects the intermediate formation steps. Our study proposes an efficient strategy to down select an optimal configuration for the mixed-functionalized surface coverage on Sc_2C *MX*ene for CO_2 activation. We strongly believe that such a strategy can be useful to guide the choice of optimal surface functionalization for efficient CO_2 reduction in other 2D materials.

ACKNOWLEDGMENTS

A.A. acknowledges the National Centre for Photovoltaic Research and Education (NCPRE) Phase II for partial funding to support this research. A.Y. acknowledges IIT Bombay for providing post-doctoral fellowship and computational resources to pursue this work. N.S. acknowledges the financial support from the Khalifa University of Science and Technology through the startup grant FSU-2020-11/2020.

[1] E. V. Kondratenko, G. Mul, J. Baltrusaitis, G. O. Larrazábal, and J. Pérez-Ramírez, Status and perspectives of CO_2 conversion into fuels and chemicals by catalytic, photocatalytic and electrocatalytic processes, Energy Environ. Sci. **6**, 3112 (2013).

[2] W. A. Thompson, E. Sanchez Fernandez, and M. M. Maroto-Valer, Review and analysis of CO_2 photoreduction kinetics, ACS Sustainable Chem. Eng. **8**, 4677 (2020).

[3] C. Xiao and J. Zhang, Architectural design for enhanced C2 product selectivity in electrochemical CO_2 reduction using Cu-based catalysts: a review, ACS Nano **15**, 7975 (2021).

[4] A. A. Peterson, F. Abild-Pedersen, F. Studt, J. Rossmeisl, and J. K. Nørskov, How copper catalyzes the electroreduction of carbon dioxide into hydrocarbon fuels, Energy Environ. Sci. **3**, 1311 (2010).

[5] C. Shi, H. A. Hansen, A. C. Lausche, and J. K. Nørskov, Trends in electrochemical CO_2 reduction activity for open and close-packed metal surfaces, Phys. Chem. Chem. Phys. **16**, 4720 (2014).

[6] X. Liu, J. Xiao, H. Peng, X. Hong, K. Chan, and J. K. Nørskov, Understanding trends in electrochemical carbon dioxide reduction rates, Nat. Commun. **8**, 1 (2017).

[7] K. P. Kuhl, E. R. Cave, D. N. Abram, and T. F. Jaramillo, New insights into the electrochemical reduction of carbon dioxide on metallic copper surfaces, Energy Environ. Sci. **5**, 7050 (2012).

[8] C. S. Chen, A. D. Handoko, J. H. Wan, L. Ma, D. Ren, and B. S. Yeo, Stable and selective electrochemical reduction of carbon dioxide to ethylene on copper mesocrystals, Catal. Sci. Technol. **5**, 161 (2015).

[9] J. D. Goodpaster, A. T. Bell, and M. Head-Gordon, Identification of possible pathways for C–C bond formation during electrochemical reduction of CO_2: new theoretical insights from an improved electrochemical model, J. Phys. Chem. Lett. **7**, 1471 (2016).

[10] K. P. Kuhl, T. Hatsukade, E. R. Cave, D. N. Abram, J. Kibsgaard, and T. F. Jaramillo, Electrocatalytic conversion of carbon dioxide to methane and methanol on transition metal surfaces, J. Am. Chem. Soc. **136**, 14107 (2014).

[11] Z. Kovacic, B. Likozar, and M. Hus, Photocatalytic CO_2 reduction: a review of ab initio mechanism, kinetics, and multiscale modeling simulations, ACS Catal. **10**, 14984 (2020).

[12] D. Kim, C. S. Kley, Y. Li, and P. Yang, Copper nanoparticle ensembles for selective electroreduction of CO_2 to C2–C3 products, Proc. Nat. Acad. Sci. **114**, 10560 (2017).

[13] P. B. O'Mara, P. Wilde, T. M. Benedetti, C. Andronescu, S. Cheong, J. J. Gooding, R. D. Tilley, and W. Schuhmann, Cascade reactions in nanozymes: spatially separated active sites inside Ag-core–porous-Cu-shell nanoparticles for multistep carbon dioxide reduction to higher organic molecules, J. Am. Chem. Soc. **141**, 14093 (2019).

[14] D. Ren, B. S.-H. Ang, and B. S. Yeo, Tuning the selectivity of carbon dioxide electroreduction toward ethanol on oxide-derived Cu_xZn catalysts, ACS Catal. **6**, 8239 (2016).

[15] S. Zhu and M. Shao, Surface structure and composition effects on electrochemical reduction of carbon dioxide, J. Solid State Electrochem. **20**, 861 (2016).

[16] M. A. Hope, A. C. Forse, K. J. Griffith, M. R. Lukatskaya, M. Ghidiu, Y. Gogotsi, and C. P. Grey, NMR reveals the surface functionalisation of Ti_3C_2 MXene, Phys. Chem. Chem. Phys. **18**, 5099 (2016).

[17] J. Yang, M. Naguib, M. Ghidiu, L.-M. Pan, J. Gu, J. Nanda, J. Halim, Y. Gogotsi, and M. W. Barsoum, Two-dimensional Nb-based M_4C_3 solid solutions (MXenes), J. Am. Ceram. Soc. **99**, 660 (2016).

[18] B. Anasori, Y. Xie, M. Beidaghi, J. Lu, B. C. Hosler, L. Hultman, P. R. Kent, Y. Gogotsi, and M. W. Barsoum, Two-dimensional, ordered, double transition metals carbides (mxenes), ACS Nano **9**, 9507 (2015).

[19] M. Asadi, K. Kim, C. Liu, A. V. Addepalli, P. Abbasi, P. Yasaei, P. Phillips, A. Behranginia, J. M. Cerrato, and R. Haasch, *et al.*, Nanostructured transition metal dichalcogenide electrocatalysts for CO_2 reduction in ionic liquid, Science **353**, 467 (2016).

[20] J. L. Hart, K. Hantanasirisakul, A. C. Lang, B. Anasori, D. Pinto, Y. Pivak, J. T. van Omme, S. J. May, Y. Gogotsi, and M. L. Taheri, Control of MXenes' electronic properties through termination and intercalation, Nat. Commun. **10**, 1 (2019).

[21] R. Ibragimova, M. J. Puska, and H.-P. Komsa, pH-dependent distribution of functional groups on titanium-based MXenes, ACS Nano **13**, 9171 (2019).

[22] B. Anasori, M. R. Lukatskaya, and Y. Gogotsi, 2D metal carbides and nitrides (MXenes) for energy storage, Nat. Rev. Mater. **2**, 1 (2017).

[23] K. Huang, C. Li, H. Li, G. Ren, L. Wang, W. Wang, and X. Meng, Photocatalytic applications of two-dimensional Ti_3C_2 MXenes: a review, ACS Appl. Nano Mater. **3**, 9581 (2020).

[24] Z. You, Y. Liao, X. Li, J. Fan, and Q. Xiang, State-of-the-art recent progress in mxene-based photocatalysts: a comprehensive review, Nanoscale **13**, 9463 (2021).

[25] Y. Xiao and W. Zhang, High throughput screening of M_3C_2 MXenes for efficient CO_2 reduction conversion into hydrocarbon fuels, Nanoscale **12**, 7660 (2020).

[26] Z. Guo, Y. Li, B. Sa, Y. Fang, J. Lin, Y. Huang, C. Tang, J. Zhou, N. Miao, and Z. Sun, M_2C-type MXenes: Promising catalysts for CO_2 capture and reduction, Appl. Surf. Sci. **521**, 146436 (2020).

[27] N. Li, X. Chen, W.-J. Ong, D. R. MacFarlane, X. Zhao, A. K. Cheetham, and C. Sun, Understanding of electrochemical mechanisms for CO_2 capture and conversion into hydrocarbon fuels in transition-metal carbides (MXenes), ACS Nano **11**, 10825 (2017).

[28] X. Zhang, Z. Zhang, J. Li, X. Zhao, D. Wu, and Z. Zhou, Ti_2CO_2 MXene: a highly active and selective photocatalyst for CO_2 reduction, J. Mater. Chem. A **5**, 12899 (2017).
[29] A. D. Handoko, K. H. Khoo, T. L. Tan, H. Jin, and Z. W. Seh, Establishing new scaling relations on two-dimensional MXenes for CO_2 electroreduction, J. Mater. Chem. A **6**, 21885 (2018).
[30] H. Chen, A. D. Handoko, J. Xiao, X. Feng, Y. Fan, T. Wang, D. Legut, Z. W. Seh, and Q. Zhang, Catalytic effect on CO_2 electroreduction by hydroxyl-terminated two-dimensional MXenes, ACS Appl. Mater. Interfaces **11**, 36571 (2019).
[31] A. D. Handoko, H. Chen, Y. Lum, Q. Zhang, B. Anasori, and Z. W. Seh, Two-dimensional titanium and molybdenum carbide MXenes as electrocatalysts for CO_2 reduction, Iscience **23**, 101181 (2020).
[32] Q. Sun, Z. Li, D. J. Searles, Y. Chen, G. Lu, and A. Du, Charge-controlled switchable CO_2 capture on boron nitride nanomaterials, J. Am. Chem. Soc. **135**, 8246 (2013).
[33] L. M. Azofra, D. R. MacFarlane, and C. Sun, An intensified π-hole in beryllium-doped boron nitride meshes: its determinant role in CO_2 conversion into hydrocarbon fuels, Chem. Commun. **52**, 3548 (2016).
[34] Y. Luo, Y. Cui, M. Li, X. Zhang, Y. Dai, C. Ling, and Y. Huang, Density functional theory investigation of structure–activity relationship for efficient electrochemical CO_2 reduction on defective $SnSe_2$ nanosheets, ACS Appl. Nano Mater. **4**, 2760 (2021).
[35] J.-Y. Liu, X.-Q. Gong, and A. N. Alexandrova, Mechanism of CO_2 photocatalytic reduction to methane and methanol on defected anatase TiO_2 (101): a density functional theory study, J. Phys. Chem. C **123**, 3505 (2019).
[36] G. Kresse and J. Furthmüller, Efficient iterative schemes for ab initio total-energy calculations using a plane-wave basis set, Phys. Rev. B **54**, 11169 (1996).
[37] G. Kresse and D. Joubert, From ultrasoft pseudopotentials to the projector augmented-wave method, Phys. Rev. B **59**, 1758 (1999).
[38] J. P. Perdew and W. Yue, Accurate and simple density functional for the electronic exchange energy: generalized gradient approximation, Phys. Rev. B **33**, 8800 (1986).
[39] J. P. Perdew, K. Burke, and M. Ernzerhof, Generalized gradient approximation made simple, Phys. Rev. Lett. **77**, 3865 (1996).
[40] P. E. Blöchl, Projector augmented-wave method, Phys. Rev. B **50**, 17953 (1994).
[41] J. D. Pack and H. J. Monkhorst, "Special points for brillouin-zone integrations"–a reply, Phys. Rev. B **16**, 1748 (1977).
[42] H. J. Monkhorst and J. D. Pack, Special points for Brillouin-zone integrations, Phys. Rev. B **13**, 5188 (1976).
[43] R. F. Bader, Atoms in molecules, Acc. Chem. Res. **18**, 9 (1985).
[44] G. Henkelman, A. Arnaldsson, and H. Jónsson, A fast and robust algorithm for bader decomposition of charge density, Comput. Mater. Sci. **36**, 354 (2006).
[45] J. Klimeš, D. R. Bowler, and A. Michaelides, Van der Waals density functionals applied to solids, Phys. Rev. B **83**, 195131 (2011).
[46] M. Dion, H. Rydberg, E. Schröder, D. C. Langreth, and B. I. Lundqvist, Van der Waals density functional for general geometries, Phys. Rev. Lett. **92**, 246401 (2004).
[47] J. K. Nørskov, J. Rossmeisl, A. Logadottir, L. Lindqvist, J. R. Kitchin, T. Bligaard, and H. Jonsson, Origin of the overpotential for oxygen reduction at a fuel-cell cathode, J. Phys. Chem. B **108**, 17886 (2004).
[48] A. Thore and J. Rosén, An investigation of the in-plane chemically ordered atomic laminates $(Mo_{2/3}Sc_{1/3})_2AlC$ and $(Mo_{2/3}Y_{1/3})_2AlC$ from first principles, Phys. Chem. Chem. Phys. **19**, 21595 (2017).
[49] K. Xiong, P. Wang, G. Yang, Z. Liu, H. Zhang, S. Jin, and X. Xu, Functional group effects on the photoelectronic properties of MXene (Sc_2CT_2, $T = O, F, OH$) and their possible photocatalytic activities, Sci. Rep. **7**, 1 (2017).
[50] See Supplemental Material http://link.aps.org/supplemental/10.1103/PhysRevApplied.18.024020 for details of total energy of the fully functionalized (O, OH, and F) Sc_2C, total and partial density of states of C and O of isolated CO_2 molecule, schematic diagram of Sc_2C structure showing the nearest neighbor of an active site, and top view of geometrically optimized CO_2 adsorption on Sc_2C-mix-*n*OH(1–6).
[51] M. Khazaei, M. Arai, T. Sasaki, C.-Y. Chung, N. S. Venkataramanan, M. Estili, Y. Sakka, and Y. Kawazoe, Novel electronic and magnetic properties of two-dimensional transition metal carbides and nitrides, Adv. Funct. Mater. **23**, 2185 (2013).
[52] V. Wang, N. Xu, J.-C. Liu, G. Tang, and W.-T. Geng, VASPkit: a user-friendly interface facilitating high-throughput computing and analysis using VASP code, Comput. Phys. Commun. **267**, 108033 (2021).